Chapter 4 Identifying hydroclimatic relationships

Persistent climate modes influence global hydrological observations. Statistical tests such as those discussed in Section 3.1.1 can identify persistence in rainfall and streamflow time series, in terms of wet and dry spells. As noted previously, the El Niño Southern Oscillation (ENSO) is the dominant global circulation phenomenon influencing the hydrologic regime of much of Australia. Previous studies have shown evidence for hydrological persistence in time series of annual rainfall in Australia, linking this characteristic to climatic regimes such as ENSO. However with ENSO phases having a mean length of approximately 15 months, the impact of this variability on hydrologic observations will be more evident by using time series of monthly totals. Climate indices are used in this chapter to demonstrate the relationships between global climate modes and hydrologic responses. Furthermore an analysis of arid-zone hydrologic data is undertaken to determine the influence of ENSO fluctuations upon the timing and magnitude of discrete flow events.

4.1 Hydrologic data

4.1.1 Spatially-averaged rainfall data

Rainfall across Australia is investigated at a monthly scale through time series that are derived from the spatial aggregation of point rainfall series and represent the varying climatic zones of Australia. Spatially-averaged rainfall data effectively describe broad-scale hydroclimatic variability by representing information over areas that share common seasonal rainfall regimes. By minimising the influence of localised sampling "noise", these totals may provide stronger evidence for anomalous climate modes such as ENSO than offered by individual station records.

Australia has extensive tropical, subtropical, and mid-latitude climate regimes that are well observed by a high quality national rain gauge network. The Australian Bureau of Meteorology (BOM) maintains up to 6000 individual rain gauges that measure accumulated rainfall totals over 24-hour periods. With rainfall data being crucial for a range of operational demands such as water storage, primary production and resource management, the use of spatially-averaged rainfall has become an integral part of the BOM's rainfall monitoring program (Jones and Beard, 1998). In the early 1900s, the BOM divided the Australian continent into geographic districts of similar climatic regimes in order to detail trends in rainfall across broad areas. The distribution of the 107 districts across the continent is shown in Figure 4.1.

Figure 4.1 Map of Australian meteorological districts

Spatially-averaged rainfall totals for each district are evaluated as the arithmetic mean of a sample of stations chosen to provide a reasonable geographical spread across the district. The reliability of data for each district are generally ensured through local knowledge (Chappel, 1995). These spatial data provide a robust measure of the meso- to synoptic-scale rainfall patterns across the continent. For most districts, monthly totals are available over the period 1913-2002, which provides 90 years of continuous values. Districts that have less than 90 years of continuous data are two districts in the Northern Territory, 14BC and 14F, which have monthly records beginning in 1925 and 1923 respectively. District-averaged series have been used in a variety of studies (eg Allan and Haylock, 1993; Drosdowsky, 1993a; 1993b) that demanded a functional description of rainfall variability across the country.

The BOM makes it clear that the daily rainfall data provided from each of their rainfall monitoring sites, which have been used to generate the district-averaged data, may contain missing data. The BOM notes that

> "Very few measuring sites have a completely uninterrupted historical record, with no gaps. Such gaps or missing data may be due to many reasons, ranging from illness of the observer to a broken instrument. A site may have been closed, reopened, upgraded or downgraded during its existence, possibly causing breaks in the record of any particular element. The station listing provides an estimate of the percentage completeness of the record for each site. The majority of

historical rainfall records have a resolution of 0.2mm although more recent measurements are resolved to 0.1mm. A total that is less than 0.1 mm (originally 0.2mm) is usually referred to as a trace. Observations are made at 9am local time. Daylight Saving has been used in some, but not all, states of Australia, since about 1973. The changeover occurs almost always in October and March but the exact dates vary from state to state and year to year. Thus the times that the totals were recorded are generally a combination of 8am and 9am times.

None of the 107 monthly district-averaged rainfall series contain missing values, although some of the daily data from measuring stations that was used to derive the former may contain missing values. Generally these daily series have been subject to quality-control by the BOM, and no further quality control was undertaken following data acquisition.

The mean monthly rainfall for the array of Australian districts ranges from 15.6mm in District 17 up to 189.7mm in District 97. Also, the coefficient of variation for these samples, taken as the ratio of the sample mean to the sample standard deviation ranges from 0.47 in District 97 to 1.69 in District 5, and the skew of monthly observations range from a minimum of 0.535 in District 89 up to 3.799 in District 46. These statistics demonstrate the considerable variability within the rainfall regime of this country.

The Australian continent can be divided into four broad rainfall regimes; the monsoonal north and northeast coast with wet summers and dry winters, the Mediterranean climate of the south and southwest coasts dominated by wet winters and dry summers, regions to the east and south east that are generally wet all year, and the dry interior in which annual rainfall is low and highly variable. In this study, the monthly rainfall series from four meteorological districts in Australia are analysed. These rainfall series are indicative of the four broad rainfall regimes that exist across this country; with District 9A having a Mediterranean climate, 27 a tropical, 16 experiencing low rainfall throughout the year and rainfall in 71 being consistently high across all twelve months. Statistics for the observed rainfall in these districts are presented in Table 4.1, which demonstrates the varying characteristics of these four climate regimes.

Table 4.1 Sample statistics for selected district-averaged monthly rainfall series

District	Mean rainfall (mm)	Median rainfall (mm)	Standard deviation	Skew
9A	73.94	58.55	61.53	0.968
16	16.15	11.2	17.04	2.255
27	122.30	30.2	155.62	1.256
71	72.19	65.0	44.71	1.003

Rainfall records from these four climatic regimes display characteristic seasonal patterns, which are demonstrated in the distribution of monthly averages in Figure 4.2.

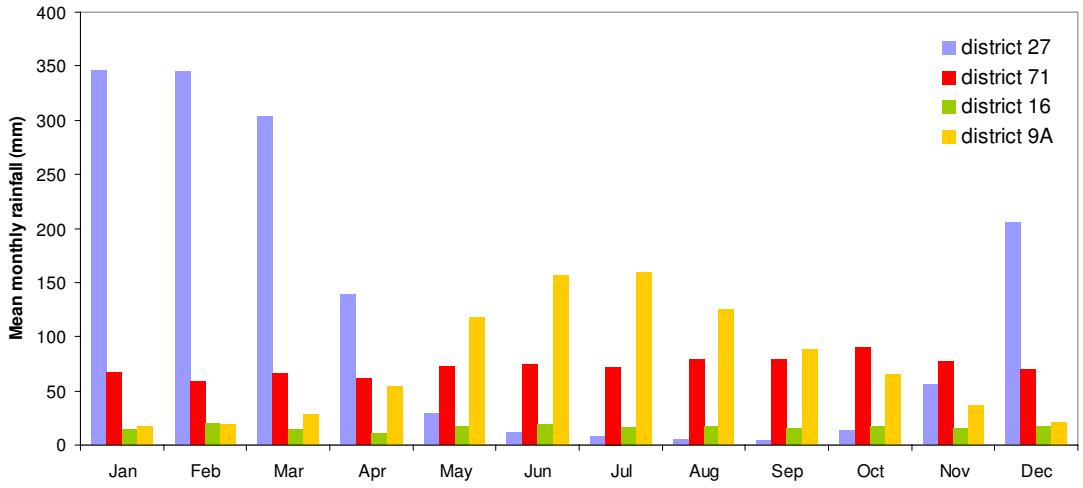

Figure 4.2 Distributions for monthly rainfall in selected meteorological districts

Prior to comparing these monthly data to sources of climate variability, the seasonal nonstationarity demonstrated in Figure 4.2 is removed. Monthly rainfall anomalies are produced by subtracting monthly means from observed values and dividing by the monthly standard deviations. This produces time series of zero mean and unit variance. These deseasonalised data are then scaled to produce time series of positive values, which is necessary to show the deseasonalised monthly variates on lognormal probability plots. This scaling is achieved by multiplying each deseasonalised value by a constant and then adding a second constant. The magnitudes of these constants are only important through the positive shift on the distribution that is produced. After completing this scaling procedure on each of the four monthly series, Anderson-Darling (AD) goodness-of-fit statistics (from Stephens, 1974) are evaluated and shown in Table 4.2.

Table 4.2 Anderson-Darling statistics for various probability distributions fitted to deseasonalised monthly rainfall

District	Gamma distribution	Lognormal distribution	Gaussian distribution
9A	5.238	1.705	17.608
16	8.572	1.312	48.368
27	17.494	8.977	32.657
71	0.387	1.660	14.227

For time series of length 1080, AD values less than 0.787 are consistent ($p = 0.05$) with data having been drawn from the selected parametric distribution. It is apparent that the deseasonalised monthly rainfall for Districts 9A and 16 are best approximated by lognormal distributions, with District 71 monthly anomalies being consistent with random draws from a gamma distribution. The scaled deseasonalised monthly values of District 27 are better

approximated by a lognormal distribution than either gamma or Gaussian distributions, although the goodness-of-fit statistic well exceeds levels of significance. The three-parameter log-Pearson III (LPIII) distribution produces an AD statistic of 6.093, which is superior to a lognormal distribution, although still exceeding a value corresponding to significance level of $\alpha = 0.05$.

4.1.2 Streamflow data

Once again focusing upon a monthly scale, the flow records for a range of Australian rivers are also analysed for evidence of persistence. This investigation used rivers that represent a range of catchment sizes, being located across a range of climate zones, an indication of relationships between sources of climatic variability and streamflow persistence are presented.

The Murray-Darling basin (MDB) is the largest river basin in Australia, draining 1.073 million km^2 of 14% of the entire land mass, as shown in Figure 4.3. The basin includes the country's two longest rivers, namely the Darling, rising in sub-tropical Queensland, and the Murray, rising in southeastern New South Wales. The MDB covers a range of climatic regimes; 80-90% of its area is arid or semi-arid with most of its runoff generated from rainfall and snowmelt in the eastern catchments. Total runoff in the MDB is merely 4% of annual rainfall, the remaining 96% being lost through evapotranspiration and infiltration. The MDB has extensive agricultural demands, and the flow regimes of the Murray and Darling rivers have been altered dramatically over the past century to support this. Estimated natural monthly flows in both rivers have been obtained with the Murray-Darling Basin Commission's Monthly Simulation Model. Flows are calculated through the addition of observable flow and diversions and losses associated with upstream storages, with estimated natural flows obtained by setting diversions from the system and the storages to zero. Total flows for the MDB are estimated at Lock 10, immediately downstream of the confluence between the Darling and Murray at Wentworth, New South Wales, and Darling flows are estimated at Burtundy. Murray flows above Lock 10 are estimated by subtracting Darling flow from total Murray-Darling flow at Wentworth. Time series of reconstructed natural monthly flows in both the Murray and the Darling are available for 108 years from January 1892 to December 1999.

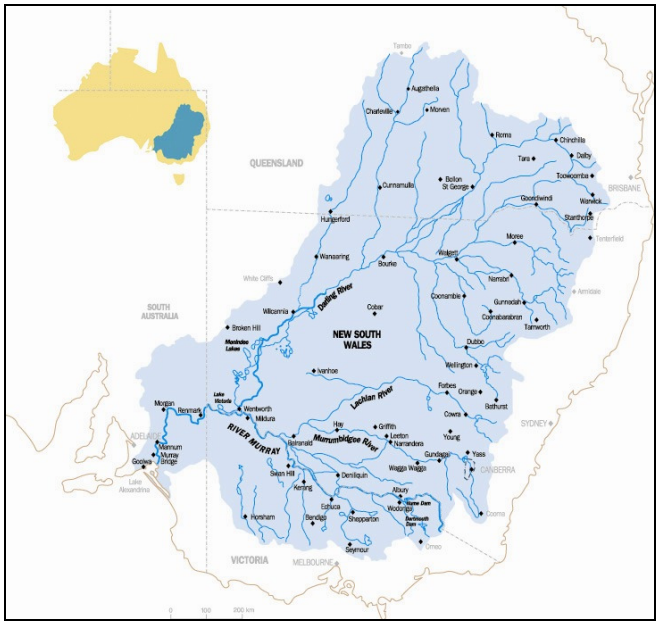

Figure 4.3 Map of the Murray-Darling basin (source: Murray-Darling Basin Commission)

The time series of natural flows in the Murray and Darling represent the runoff from a very large catchment area that covers various geographical regions of Australia. Runoff from this basin may represent either widespread or localised rainfall events. In order to investigate whether climatic persistence influences flows from smaller catchments, monthly streamflows from two rivers in southeastern Queensland, within the headwaters of the MDB are also analysed. The hydrology of both rivers is highly variable, being dominated by a summer rainfall regime. The Dumaresq River is located within the Border Rivers catchment, west of the Great Dividing Range on the Queensland-New South Wales border, and has a sub-catchment of approximately 10,000 km^2. Monthly flows in this river are available for the period (1954-1987). The Condamine River catchment is located to the north of the Dumaresq, and is bordered by the Great Diving Range to the east and the north, covering an area of over 13,000 km^2. The Condamine is the source of the longest continuous stretch of river in the MDB, extending over 3750 km to its mouth in South Australia. Monthly flow records for the Condamine are available for the period (1947-2003).

The flow records for two rivers in the Lake Eyre basin of Australia, shown in Figure 4.4, are also investigated. This basin covers over 1.1 million km^2 of the generally arid central zone of Australia, having a mean annual runoff that is the lowest of any major drainage basin in the world (Kotwicki and Allan, 1998). The Diamantina River and Cooper Creek display a high variability in the duration and volume of discharges that is characteristic of arid zone rivers. The Diamantina River is located in southwestern Queensland and its catchment covers approximately 120,000 km^2. Monthly flow records for the Diamantina at the Queensland town of Birdsville, 10 km from the northern border of South Australia, are available over the period

(1966-2002). Cooper Creek has a larger sub-catchment, covering an area of approximately 306,000 km^2, most of which is located upstream of the Cullyamurra gauging station in South Australia. Monthly flow records are available over 29 years during the period (1973-2001).

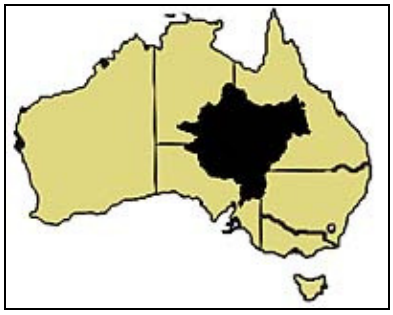

Figure 4.4 Location of the Lake Eyre basin (after Parliament of Australia Library, 2001)

The sixth flow record analysed is for the Burdekin River, located in tropical Queensland. This river flows over 700km before discharging in the Pacific Ocean near the town of Ayr, through a catchment of 130,000 km^2 that also has a summer-dominated rainfall regime. Monthly flow data for the river are available at the gauging station of Sellheim over the period (1947-2004). Details for these seven monthly streamflow series are presented in Table 4.3.

Table 4.3 Summary statistics for the monthly flow records of the seven rivers analysed

River (Site no.)	Area (km^2)	Latitude	Longitude	Record period	Mean (GL)	SD (GL)	Skew
Murray Darling	1057000*	34°6'S	141°55'E	(1892-1999)	1082.6 166.8	1105.5 208.6	2.25 2.27
Cooper (003501)	230000	27°42'S	140°50'E	(1973-2002)	136.3	669.3	9.59
Diamantina (002101)	120000	25°54'S	139°22'E	(1966-2002)	117.3	483.1	8.82
Burdekin (120002c)	36260	20°0'S	146°26'E	(1947-2004)	373.7	1138.8	5.68
Dumaresq (416308a)	8755	28°44'S	152°17'E	(1954-1987)	48.5	97.0	4.77
Condamine (422316a)	7795	27°33'S	151°13'E	(1947-2003)	29.8	92.1	6.59

* Area for Murray and Darling is approximate area of entire MDB, and coordinates are for Wentworth gauge

Time series of the seven monthly flow records are shown in Figure 4.5, with the high variability in the two arid zone rivers clearly apparent.

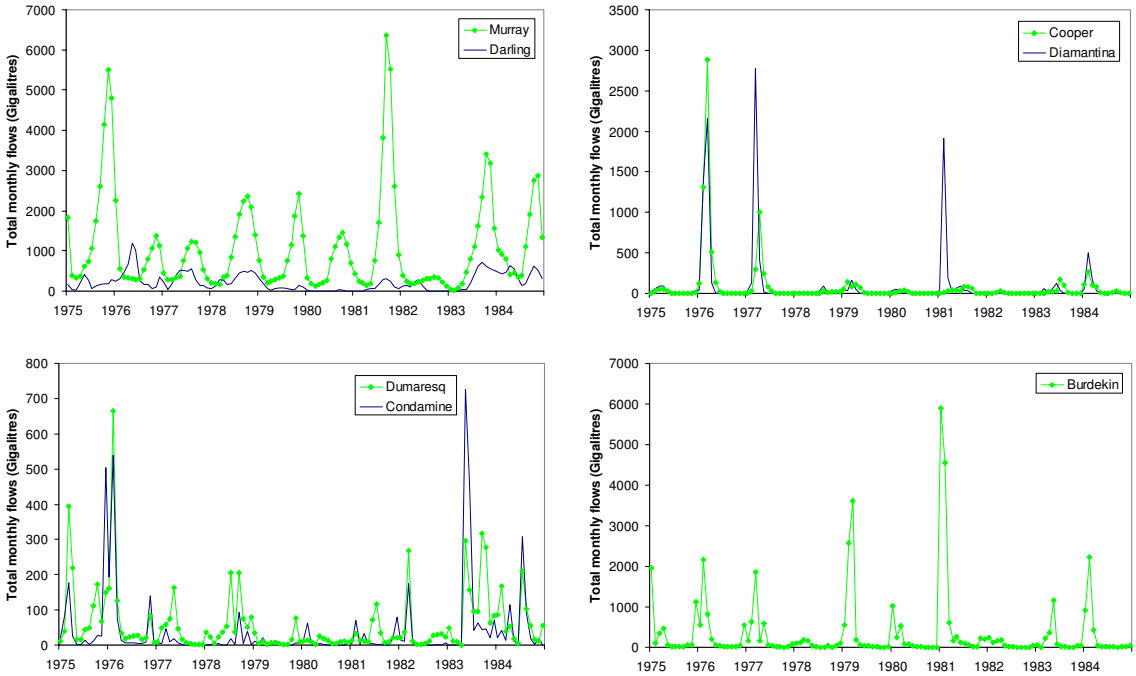

Figure 4.5 Time series of monthly flows for the seven rivers analysed, shown over 10-year periods

The statistics for flow records in each month are displayed in Table 4.4 and Table 4.5. These statistics show that each monthly streamflow series is characterised by seasonal nonstationarity that is removed to produce series with zero mean and unit variance prior to analysing the relationship with climate indices.

Table 4.4 Summary statistics for the seven flow records from January to June

		Jan	Feb	Mar	Apr	May	Jun
Murray	Mean	716.0	384.9	291.5	315.4	469.9	712.1
	SD	586.6	235.7	170.9	227.8	368.8	550.8
	Skew	1.89	1.30	1.28	2.46	2.66	3.31
Darling	Mean	146.0	140.6	157.1	183.1	183.5	149.0
	SD	179.5	170.4	160.2	187.6	209.2	219.1
	Skew	1.73	2.36	1.06	1.33	1.73	3.03
Cooper	Mean	90.1	415.5	264.7	197.8	287.0	207.4
	SD	283.6	1706.3	753.7	403.9	1036.0	673.3
	Skew	4.76	5.21	3.49	3.03	5.06	3.68
Diamantina	Mean	154.4	415.6	454.2	178.0	74.2	50.9
	SD	406.1	1241.2	807.5	383.7	180.1	150.7
	Skew	3.59	4.82	1.87	2.72	3.03	3.81
Burdekin	Mean	1172.5	1446.1	1137.5	233.7	117.1	48.2
	SD	2391.5	1935.1	1667.9	332.0	249.2	96.8
	Skew	3.22	2.20	2.23	1.98	4.05	4.17
Dumaresq	Mean	82.5	88.4	50.5	24.3	30.6	29.9
	SD	150.2	202.3	82.2	44.4	62.0	60.9
	Skew	3.49	3.33	3.03	3.21	3.16	3.62
Condamine	Mean	44.1	59.6	34.1	35.2	44.8	29.8
	SD	93.4	135.8	68.1	156.3	153.2	83.3
	Skew	2.68	3.41	3.30	7.18	4.56	3.99

Table 4.5 Summary statistics for the seven flow records from July to December

		Jul	Aug	Sep	Oct	Nov	Dec
Murray	Mean	1096.7	1560.8	1997.6	2172.2	1929.3	1344.1
	SD	765.1	1070.5	1312.6	1370.3	1363.1	1115.1
	Skew	3.24	2.72	1.78	1.18	1.42	1.66
Darling	Mean	132.5	165.1	190.2	202.9	189.4	161.8
	SD	203.8	220.1	230.5	245.9	245.9	207.7
	Skew	3.08	2.43	2.43	2.39	2.23	1.71
Cooper	Mean	96.2	35.1	11.8	3.3	13.9	13.3
	SD	280.0	84.1	27.6	8.0	60.2	29.0
	Skew	3.59	3.76	3.13	3.48	5.31	3.08
Diamantina	Mean	22.6	8.9	2.4	0.7	7.8	37.3
	SD	61.7	20.6	6.8	2.0	20.3	148.4
	Skew	4.84	2.99	4.00	4.18	3.61	5.66
Burdekin	Mean	21.7	12.7	12.1	8.8	62.9	211.1
	SD	30.3	15.2	39.5	13.6	152.4	323.0
	Skew	3.53	2.89	7.04	2.37	5.12	2.76
Dumaresq	Mean	45.4	28.1	42.5	54.0	51.4	54.9
	SD	72.1	32.4	67.4	94.1	66.5	86.8
	Skew	2.49	2.06	2.83	3.10	1.75	2.50
Condamine	Mean	22.4	11.2	6.7	17.9	19.8	31.8
	SD	57.4	24.4	16.4	49.9	38.0	78.0
	Skew	3.83	3.65	4.00	3.48	2.64	4.59

4.2 Relationships between hydrology and climate indices

4.2.1 Influence of ENSO upon rainfall

The impact of ENSO on the synoptic conditions of Australia is demonstrated through the influence of its variability upon the mean value of monthly rainfall anomalies. Monthly totals are used here in preference to annual aggregations due to the average duration of ENSO events being 15 months, thus annual totals may conceal the influence of this ENSO signal.

The five-month running mean (5-mrm) values of the NINO3 index is used to classify months as being either La Niña, ENSO neutral or El Niño, using thresholds of ±0.4^{o}C. For the 1080 months (1913-2002) over which district-averaged rainfall is available, 320 months are defined as being El Niño, 267 La Niña and the reminder classified as neutral. Deseasonalised rainfall totals in El Niño months are compared to values associated with La Niña months. An independent 2-sample *t*-test can determine whether the opposite phases of ENSO are associated with statistically significant differences in the mean value of rainfall in each district, when the population standard deviations of each phase are unknown. A significance interval around the difference in sample means is obtained together with a *p*-value associated with this test statistic. The significance of the difference in mean is tested at a 5% level.

The results from fitting 2-sample *t*-tests to the various deseasonalised monthly rainfall series are shown in Table 4.6. The results are shown alongside the linear correlations between monthly values of the NINO3 index and the monthly rainfall anomalies, together with the significance

probabilities for both statistics. The four district-averaged series are all significantly correlated to the monthly NINO3 series, and show significantly higher means during La Niña periods, with District 27 having the strongest correlations with NINO3 and also the greatest modulation between ENSO phases. These results suggest that the hydrologic influence of ENSO is not limited to the eastern coastal regions of Australia.

Table 4.6 Results for 2-sample t-tests and linear correlations between deseasonalised monthly rainfall and monthly NINO3, with associated probabilities, for four district-averaged rainfall series

District	Mean difference (95% CI)	Probability	Correlation to NINO3	Probability
9A	**0.419** (0.589, 0.249)	< 0.001	-0.123	< 0.001
16	**0.242** (0.406, 0.078)	0.004	-0.080	0.008
27	**0.583** (0.738, 0.428)	< 0.001	-0.199	< 0.001
71	**0.213** (0.376, 0.049)	0.011	-0.101	0.001

The linear correlations shown in Table 4.6 are very small, with the NINO3 series explaining less than 4% of the variability in these monthly rainfall series. However it is likely that this hydroclimatic relationship will underlie stronger correlations in streamflow data, which is investigated in Section 4.2.4. It is possible though to investigate the seasonality in the interaction between ENSO and district-averaged rainfall, by calculating linear correlations for each calendar month, as shown in Figure 4.6. These district-averaged rainfall data have 90 values in each calendar month, and correlations over this sample size that have absolute magnitude greater than 0.208 are statistically significant at a 5% level. The correlations in Figure 4.6 show a slight tendency towards ENSO having a stronger influence on rainfall in Districts 16, 27 and 71 throughout the summer months as opposed to winter months. This seasonal bias is less apparent in District 9A.

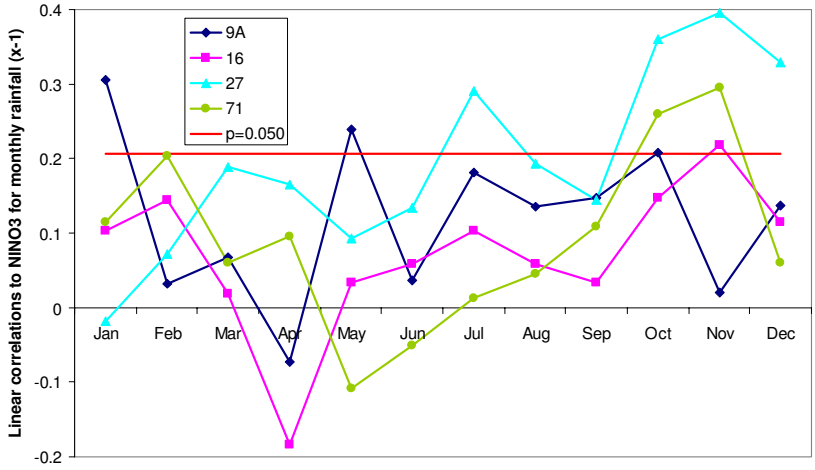

Figure 4.6 Linear correlations between NINO3 values and deseasonalised rainfall for the four districts calculated for each calendar month (multiplied by -1), with solid line indicating the magnitude of statistically significant correlation

To further understand the relationship between Pacific climate variability and rainfall across Australia, relationships between the NINO3 index and the 107 district-averaged rainfall series are now established. This investigation shows 90 of the 107 districts (84%) to have statistically significant correlations $(p < 0.05)$ between deseasonalised monthly rainfall totals and the monthly NINO3 index. These districts are shaded in Figure 4.7. The areas failing to show significant correlation are the low rainfall areas of Western Australia and the west coast of Tasmania. Hydrologic processes in these two regions may be modulated to a greater degree by climatic influences derived from either the Indian or Southern Oceans (eg Kuhnel, 1990). Although the monthly rainfall series for 90 districts are significantly predicted by NINO3, it is important to note that for the rainfall series that is best predicted (District 27 in north Queensland), this index can explain only 4% of total variability. This demonstrates that various other climate phenomena may be at least as important for explaining variability in monthly rainfall.

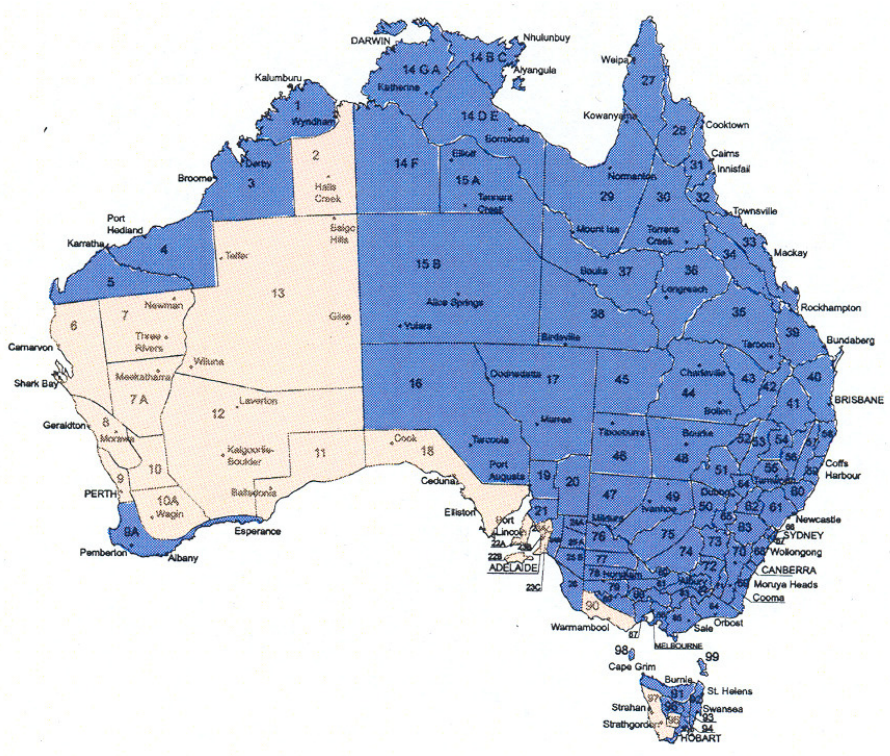

Figure 4.7 Districts that show statistically significant linear correlation between deseasonalised monthly rainfall and monthly NINO3 values

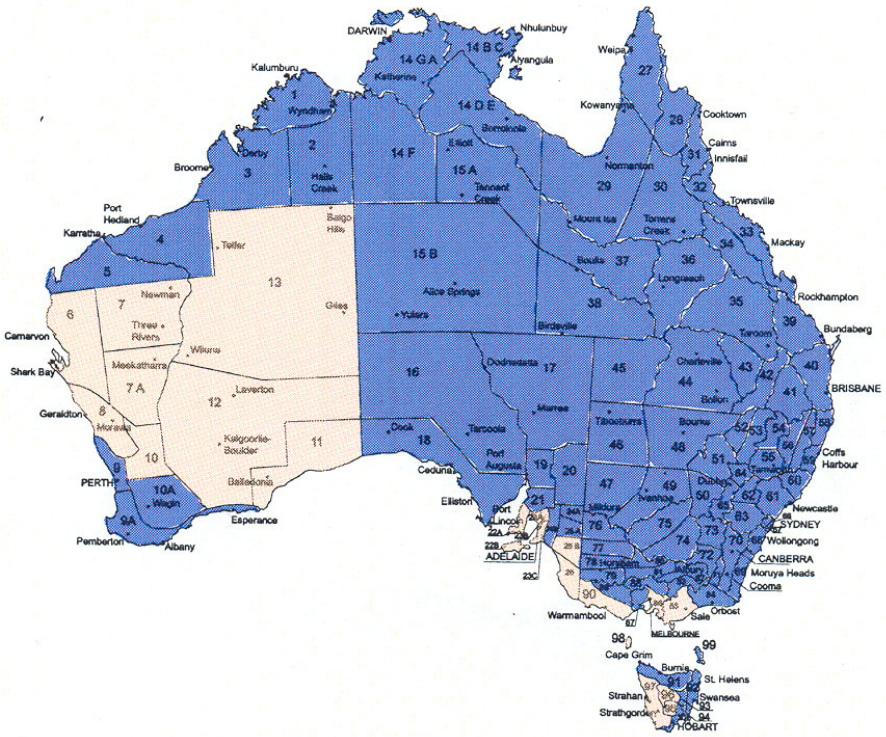

Figure 4.8 Districts that show a statistically significant difference in monthly mean rainfall between La Niña and El Niño months

After categorising months as El Niño and La Niña, 2-sample *t*-tests are again used to determine the significance of mean differences in monthly rainfall anomalies between the opposite extremes of ENSO. The districts that demonstrate a significant difference in mean $(p < 0.05)$ are shaded in Figure 4.8 and their location closely matches the regions that display significant correlation to NINO3. From this analysis, 88 districts (82%) show a significant increase in the mean rainfall anomaly for La Niña months as opposed to El Niño months. Furthermore, opposite ENSO phases produce statistically significant differences in monthly rainfall variability for 54 of the Australian districts (52%). This suggests that ENSO influences monthly rainfall across Australia, through modulating both the expected value and the variability of rainfall in a majority of meteorological districts.

A final measure of the association between ENSO and the variability of monthly rainfall across Australia is the relationship between the 2-sample *t*-test statistics and the monthly coefficient of variation (C_v) for each district. By defining C_v as the ratio of the sample standard deviation to the sample mean for the observed monthly rainfall from each district, the rank correlation $(r = 0.34)$ between these values and the t-test statistics across the 107 districts is highly significant $(p < 0.001)$.

Districts showing the greatest variability in monthly rainfall have a tendency for large differences in mean rainfall between El Niño and La Niña episodes. These results concur with numerous published results that indicate an association between ENSO phase and a widespread and substantial modulation of rainfall across much of Australia. It is clear that persistence within ENSO phases influences the rainfall regimes of Australia.

4.2.2 Influence of IPO upon rainfall

The importance of climate modes other than ENSO in the modulation of Australian rainfall is now investigated with the low frequency IPO index. By using thresholds of ±0.5 to define the positive and negative phases of the IPO (consistent with Power *et al.*, 1999a; Kiem *et al.*, 2003), the difference in mean monthly rainfall between opposite phases is analysed through 2-sample *t*-tests. Confidence intervals around the mean monthly difference for each district-averaged series are shown in Table 4.7 with significance probabilities. Together with these results, Table 4.7 shows the linear correlation (and *p*-values) between monthly rainfall and monthly IPO, where IPO values are constant for 3 consecutive months. Although Table 4.6 demonstrates a significant relationship between ENSO phase and monthly rainfall variability, the results in Table 4.7 fail to show a similar relationship for opposite IPO phases. This is an expected result as these rainfall series are 90 years in length, and IPO has multidecadal cycles. Furthermore, correlations between deseasonalised monthly rainfall and IPO are weaker than corresponding correlations to NINO3, with only District 16 being statistically significant at a 5% level.

Table 4.7 Results for 2-sample t-tests and linear correlations between deseasonalised monthly rainfall and monthly IPO values, with significance probabilities

District	Mean difference (95% CI)	Probability	Correlation to IPO	Probability
9A	**0.026** (0.129, -0.181)	0.739	-0.037	0.233
16	**0.109** (0.050, -0.267)	0.179	-0.062	0.044
27	**0.152** (0.327, -0.010)	0.065	-0.056	0.073
71	**0.120** (0.272, -0.032)	0.120	-0.054	0.079

Although monthly rainfall in these four districts was not significantly influenced by IPO, the importance of this source of climatic variability on the various rainfall regimes is now investigated using deseasonalised monthly totals. From using 2-sample *t*-tests, a majority of districts across the continent show a bias towards higher monthly rainfalls during IPO negative phases. Although 11 districts show a tendency towards lower rainfall during these periods, including Districts 4, 7, 7A, 8, 9, 10, 10A, 11 and 12 in Western Australia and 32 and 34 in Queensland, in only District 11 is this difference statistically significant. The 60 districts that show statistically significant difference in monthly rainfall due to opposite IPO phases are shaded in Figure 4.9.

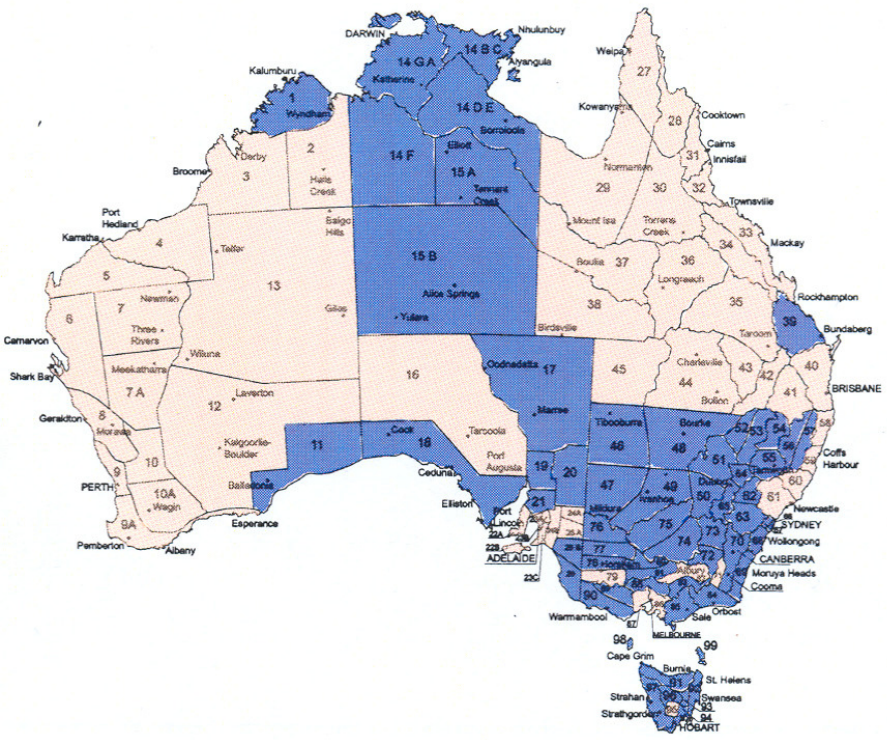

Figure 4.9 Districts that show a statistically significant difference in monthly mean rainfall between IPO+ and IPO- months

The influence of both IPO and ENSO upon the regional climate of Australia is clearly shown from the fact that 52 of the 60 shaded districts in Figure 4.9 also have a significant difference in monthly rainfall between El Niño and La Niña months. With IPO persisting in each phase for extended periods before undergoing rapid phase changes, it is clear from these results that there will be a tendency for higher or lower rainfall over multi-decadal periods. Superimposed upon this long-term persistence in rainfall are shorter-duration fluctuations due to oscillations between ENSO phases.

4.2.3 Influence of non-Pacific climate modes upon rainfall

Many existing prediction systems for Australian rainfall focus primarily upon the influence of the tropical ENSO, with little regard given to the influence of interannual SST variability in the Indian and Southern Oceans. The Australian BOM utilise the link between Pacific SST anomalies and precipitation anomalies across Australia to generate predictions over 60-90 day lead times. The Queensland Department of Primary Industries analyse phases of SOI to predict precipitation anomalies over northeast Australia (eg Stone *et al.*, 1996). In a different approach, White (2000) focused upon the eastward propagation of covarying SST and moisture flux anomalies though the Indian and Southern Oceans to predict interannual precipitation changes. This latter study demonstrated that ocean-atmospheric changes surrounding Australia can influence the distribution and magnitude of precipitation.

The role of anomalous changes in Indian Ocean SSTs, particularly those associated with the IOD, in the modulation of Australian rainfall is now investigated by assuming independence from ENSO. Partial correlations can highlight relationships between dependent variables (in this case a time series of monthly rainfall anomalies) and a predictor variable from which a second predictor has been partialled. This method was utilised by Saji and Yamagata (2003) to detail impacts of the IOD on seasonal rainfall totals across the globe. The partial correlation between the dependent variable Y and the first predictor variable X_1 is calculated as:

$$p_1 = \frac{r_{Y,1} - r_{Y,2} r_{1,2}}{\sqrt{(1 - r_{1,2}{}^2)(1 - r_{Y,2}{}^2)}} \quad \textbf{(4.1)}$$

where $r_{Y,1}$ is the linear correlation between the dependent variable and first predictor variable, and similarly for other terms. The square of this quantity, p_1^2, describes the amount of variance in the dependent series not already explained by X_2, that is explained by X_1.

In this analysis, monthly values of the NINO3 and the Indian Ocean dipole index (DMI) are used as predictors for the deseasonalised monthly rainfall series for the four meteorological districts. The correlation between the DMI and the deseasonalised monthly rainfall from which NINO3 is partialled is compared to the correlation between NINO3 and rainfall from which DMI is previously partialled. This allows the influences of both oceans upon Australian rainfall to be analysed separately. Partial correlations between monthly rainfall anomalies and the NINO3 and DMI series are displayed in Table 4.8. The DMI is shown to explain four times the variability in the monthly rainfall anomalies of District 16 than the NINO3 series, and slightly more of the variability in District 71 rainfall. In Districts 9A and 27 however, the effect of DMI is negligible once ENSO effects are removed.

Table 4.8 Partial correlations between deseasonalised monthly rainfall and monthly NINO3 when allowing for DMI and deseasonalised monthly rainfall and monthly DMI values when allowing for NINO3

District	Partial correlation to NINO3	Partial correlation to DMI
9A	-0.116	-0.013
16	-0.052	-0.103
27	-0.160	-0.050
71	-0.076	-0.086

By repeating this analysis with deseasonalised monthly rainfall in each Australian district over the period 1913-2002, 43 districts of Australia (those shaded in Figure 4.10) show the DMI to be a more significant predictor than the monthly NINO3. The spatial distribution of these shaded districts favours the southwestern half of the continent, with no district in either the

Northern Territory or Queensland, and only a few districts in New South Wales having a relationship to the IOD that improves the relationship to ENSO. Importantly, the shaded districts throughout Western Australia correspond to regions that did not show significantly lower rainfall in El Niño periods as opposed to La Niña episodes. These results show that each of the ocean basins surrounding Australia have important influences upon the variability of Australian climate. Furthermore, these results are consistent with empirical evidence that shows the IOD to influence Australian rainfall through a modulation of cloud bands that deliver rainfall in a northwest-southeast direction across the continent.

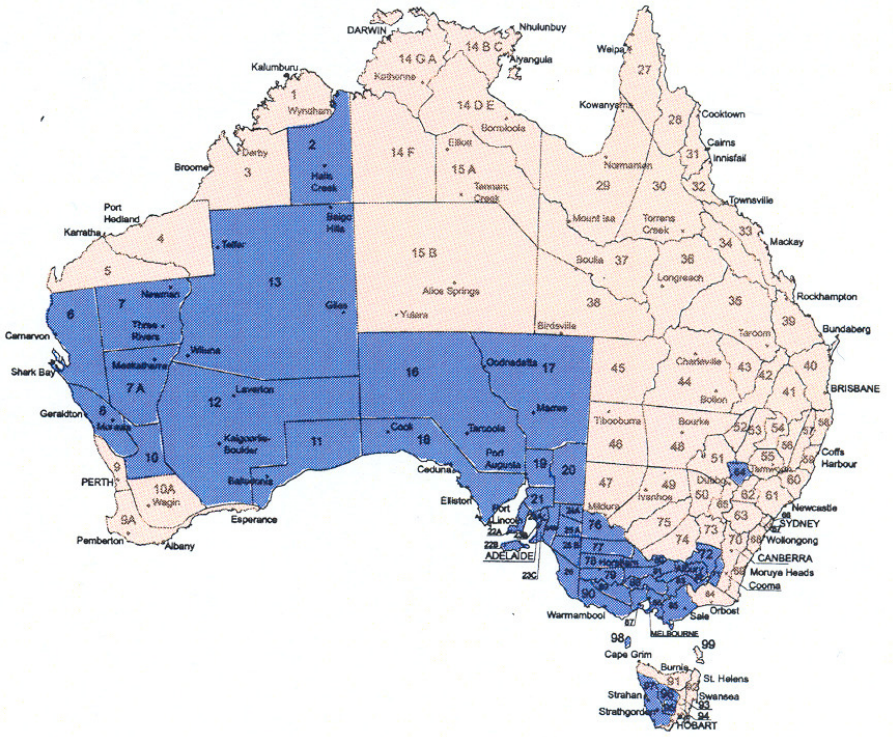

Figure 4.10 Districts in which the correlation between monthly DMI values and deseasonalised monthly rainfall from which NINO3 has been partialled exceeds the correlation between monthly NINO3 values and deseasonalised monthly rainfall from which DMI has been partialled

The cumulative impact of the ENSO, IPO and IOD on the Australian rainfall regime is now estimated through the method of Principal Component (PC) analysis. The PC method reduces the number of dimensions of the prediction data such that a smaller number of uncorrelated variables are used. Using monthly values of the NINO3, IPO and DMI indices over their common period (1869-1999), the first principal component (PC_1) accounting for 46% of the total variability in these series is evaluated as

$$PC_1 = 0.704 \times NINO3 + 0.508 \times IPO + 0.497 \times DMI \qquad \textbf{(4.2)}$$

The first PC represents an overall impact of these three climate modes, as each coefficient has the same sign and is not close to zero. This is consistent with observed patterns of the negative

phase of each mode corresponding to increased rainfall across Australia. The evaluation of PC_1 over slightly different time periods should alter the coefficients associated with each index although retaining the same signs. Eq. 4.2 may be used to generate a time series of monthly variates in order to relate with monthly rainfall anomalies. Table 4.9 compares linear correlations between the PC_1 index and the deseasonalised monthly rainfall in each of the four selected districts, with correlations between rainfall and monthly NINO3 values. These results show that the PC_1 series explains a greater amount of monthly rainfall variability in Districts 16 and 71 than NINO3, reflecting significant relationships between these data and the IOD series.

Table 4.9 Linear correlations (and significance probabilities) between deseasonalised monthly rainfall and monthly PC_1 and NINO3 values

District	Correlation to PC_1	Correlation to NINO3
9A	**-0.109** (<0.001)	**-0.123** (<0.001)
16	**-0.106** (0.001)	**-0.081** (0.008)
27	**-0.180** (<0.001)	**-0.199** (<0.001)
71	**-0.115** (<0.001)	**-0.101** (0.001)

Each of the district-averaged rainfall series from across Australia are now analysed to elucidate the amount of rainfall variability explained by the PC_1 series. For the 81 Australian districts (76% of districts) shaded in Figure 4.11, linear correlations to the PC_1 series are stronger than correlations to the NINO3 index. This clearly indicates that PC analysis provides a valuable summary of major climate modes that modulate the climate of Australia.

This section has shown evidence for widespread modulation by the dominant climate modes of monthly rainfall data from across Australia. It is likely that the interaction of these various circulation phenomena will produce a forcing mechanism in the hydrological cycle, which is revealed as persistence within a finite number of stable climate states.

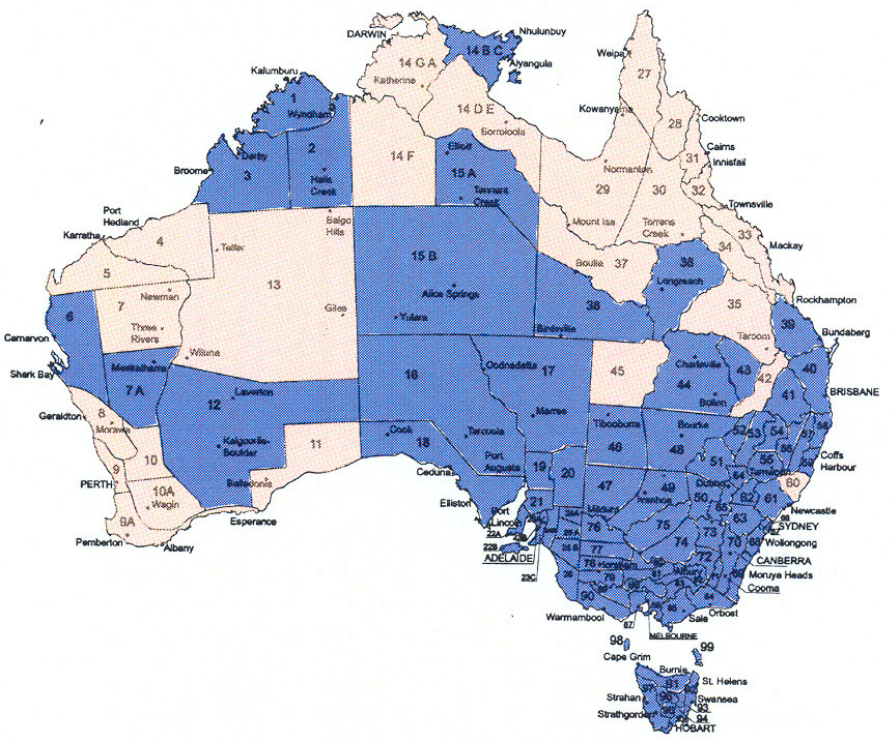

Figure 4.11 Districts in which the correlation between deseasonalised monthly rainfall and monthly PC_1 values exceeds the correlation between rainfall and monthly NINO3

4.2.4 Influence of ENSO and IPO upon streamflow

The relationships between deseasonalised monthly flow records and the ENSO and IPO phenomena are explored in this section initially through multiple linear regressions using monthly NINO3 values and monthly values of the seasonal IPO index as predictor variables. In order to represent the combined influence of these two climatic modes, the significance of the product of the NINO3 and IPO indices (referred to as *NI*) as a predictor of monthly flows is also analysed.

For the time series of deseasonalised monthly flows in the Murray (y_t), which has zero mean and unit variance, the equation having the smallest estimated standard deviation of errors is:

$$y_t = -0.121 - 0.324 \times NINO3 - 0.135 \times IPO + 0.108 \times NI \qquad \textbf{(4.3)}$$

This equation is statistically significant $(p < 0.001)$ using a t-test, and explains approximately 10.7% of the variability within the time series of deseasonalised monthly flows. The addition of the *NI* term reduces the standard deviation of errors from 0.951 to 0.947 and increases the R^2 value from 8.9%. Table 4.10 shows coefficients (with standard errors) for regressions of deseasonalised monthly flows in each river using these three predictor variables.

Table 4.10 Coefficients and standard errors for regression of deseasonalised monthly streamflows on climate indices, with R^2 values, standard deviation of residuals and significance

	Constant (SE)	NINO3 (SE)	IPO (SE)	NINO3xIPO (SE)	R^2	S	P
Murray	**-0.121** (0.053)	**-0.324** (0.034)	**-0.135** (0.026)	**0.108** (0.031)	10.7%	0.943	<0.001
Darling	**0.063** (0.027)	**-0.337** (0.034)	**-0.205** (0.026)	**0.110** (0.030)	14.0%	0.925	<0.001
Cooper	**0.077** (0.079)	**-0.278** (0.093)	**-0.081** (0.064)	**0.143** (0.075)	4.9%	0.982	0.001
Diamantina	**0.016** (0.053)	**-0.137** (0.055)	**-0.014** (0.045)	**0.020** (0.044)	1.8%	0.978	0.065
Burdekin	**-0.021** (0.039)	**-0.158** (0.044)	**-0.084** (0.034)	**0.097** (0.037)	4.2%	0.943	<0.001
Dumaresq	**-0.022** (0.052)	**-0.081** (0.059)	**-0.052** (0.052)	**0.087** (0.048)	1.8%	0.981	0.067
Condamine	**0.026** (0.042)	**-0.134** (0.048)	**-0.041** (0.037)	**0.045** (0.039)	1.8%	1.014	0.009

The three predictor variables shown in Eq. 4.3 may not necessarily produce the optimal regression equations for each streamflow time series, and the results in Table 4.10 show the combined hydrologic impact of ENSO and IPO to vary dramatically for the different catchment sizes and locations. In particular flows in the Dumaresq and Condamine, located in the southeast of Queensland, show only weak relationships to this source of climatic variability. However, when principal component analysis is used to generate a series from the same predictor variables as Eq. 4.3, these two rivers show a stronger correlation to the PC_1 series than to the NINO3 series. In the other rivers analysed, the PC_1 series explains less variability in the monthly flow series than the NINO3 series can explain alone, suggesting a stronger relationship between ENSO and monthly streamflow.

The modulation by low-frequency IPO variability of the ENSO impact on streamflow can also be analysed through a categorisation of each month in the manner shown in Table 4.11. Through considering the central category (representing neutral ENSO and neutral IPO) as a base condition, all other combinations of the El Niño, La Niña, ENSO neutral, IPO negative, IPO positive and IPO neutral phases are represented by 8 separate indicator categories. For each monthly period, the category corresponding to the specific combination of ENSO (identified by 5-mrm of the NINO3 index) and IPO takes a value of one, with each of the other seven categories taking a value of zero.

Table 4.11 Monthly climate indicator categories based on NINO3 and IPO indices

	IPO < -0.5	-0.5 < IPO < 0.5	IPO > 0.5
La Niña (NINO3-5mrm < -0.4)	1	8	7
ENSO neutral (-0.4 < NINO3-5mrm < 0.4)	2	–	6
El Niño (NINO3-5mrm > 0.4)	3	4	5

Time series of the eight climate categories are used as predictors in multiple linear regressions of the monthly streamflow records. These categories improve regression models shown in Table 4.10 (by increasing P-values and reducing standard deviation of residuals) for each river except the two located within the Lake Eyre Basin. The most significant predictors for both Murray and Darling flows are categories 1, 2 and 8, which represent predominantly La Niña conditions in IPO negative periods, a result which is consistent with the observations of Power *et al.* (1999a) described earlier.

The influence of ENSO upon monthly streamflow records is also analysed by comparing mean flows in El Niño months with mean flows in La Niña months using 2-sample t-tests. In each of the deseasonalised monthly streamflow time series, there is significant serial correlation, as shown in Table 4.12. In time series that have such characteristic, it is important to adjust the t-test to take this into account. The standard t-test would determine the difference in means of two samples ($\overline{y_1}$ and $\overline{y_2}$) by evaluating the statistic shown in

$$t = \frac{\overline{y_1} - \overline{y_2}}{\sqrt{s_1^2/n_1 + s_2^2/n_2}} \tag{4.4}$$

where s_1^2 and n_1 are the variance and numbers of values in sample 1, and same for sample 2. Where there is significant serial correlation in these samples, the test statistic has to be varied using the value of the first-order autocorrelation coefficient, $r(1)$, such that

$$\frac{s_i^2}{n_i} \rightarrow \frac{s_i^2}{n_i} \times \frac{(1 + r(1))}{(1 - r(1))} \tag{4.5}$$

The results of these modified t-tests are shown in Table 4.12, and demonstrate that mean monthly flows four of the seven rivers analysed are significantly influenced (at a 5% level) by opposing ENSO phase.

Table 4.12 Mean difference in deseasonalised monthly streamflows between opposite ENSO phases, with 90% interval for the difference and associated significance level

River	First-order autocorrelation coefficient	Mean difference between La Niña and El Niño episodes	P
Murray	0.885	**0.550** (0.001, 1.099)	0.025
Darling	0.882	**0.727** (0.196, 1.258)	0.004
Cooper	0.543	**0.452** (-0.105, 1.009)	0.057
Diamantina	0.508	**0.122** (-0.191, 0.435)	0.223
Burdekin	0.455	**0.513** (0.237, 0.790)	<0.001
Dumaresq	0.433	**0.287** (-0.116, 0.690)	0.082
Condamine	0.293	**0.485** (0.166, 0.804)	0.002

4.3 Relationships between arid zone hydrology and climate indices

As shown in the previous section, the relationship between ENSO variability and streamflow responses are almost always stronger than its relationship to rainfall (eg Chiew and McMahon, 2003). Flow events from arid zone streams are now analysed, as these may provide the most detectable response to ENSO modulation. The hydrology of arid zones is particularly interesting, with flow regimes characterised by high seasonal variation and periods of zero or very low flows. Other factors, including those associated with irregular atmospheric circulations such as ENSO have been shown to strongly influence arid zone flow patterns (eg Puckridge *et al.*, 2000). Indeed, the highly variable flow regimes of these regions potentially amplify the ENSO teleconnections observed in the less-extreme flow records of other rivers.

4.3.1 Flows in the Todd River

In this section, the flow data from the Todd River are examined. Located at the northwestern edge of the Lake Eyre basin (see Figure 4.4), the sub-catchment of the Todd River above Alice Springs covers 450 km^2. Daily flows are available for a period of 37 years (1962-1998). This river is characterised by periods of very low or zero flow, which separate distinct flow events that continue for an average of 41 days. The distinctive pattern of flow in the Todd River is shown in Figure 4.12 using a two-year sample of daily flow.

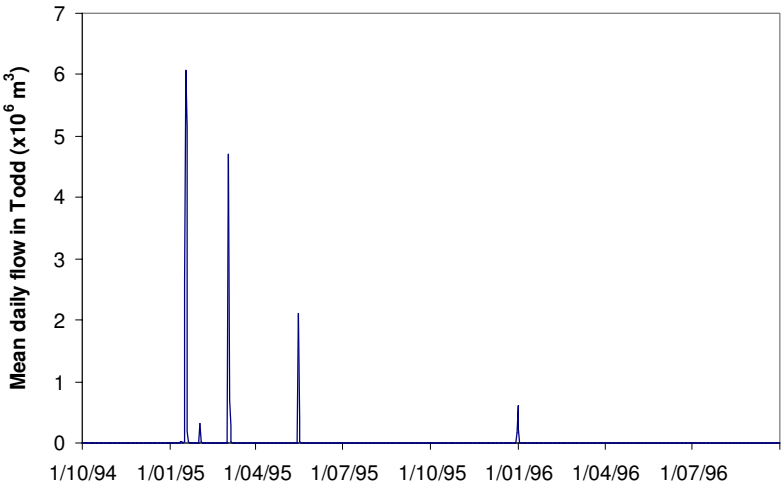

Figure 4.12 Daily flows in the Todd River (1994-1996)

In this study, flow events are referred to as *spates*, defined as a continuous sequence of days over which non-zero flow is recorded. Annual summary statistics of this flow record are presented in Table 4.13, with water years beginning October 1st. Daily flow exceeds the sample average for approximately 3% of the time, with 49% of months recording zero flow.

Table 4.13 Summary flow statistics for the Todd River

Total annual flow (x10^6 m^3)				Number of annual spates	
Minimum	Median	Mean	Maximum	Mean	Variance
0	6	11	94	3.27	4.65

The strong seasonal pattern of flow is shown in Figure 4.13, with average monthly flows expressed as a percentage of average annual flow. With large intra-annual variability, in which flows in January to March are much larger on average than flows in July to September for example, it is more appropriate to analyse variability in the annual flow regime.

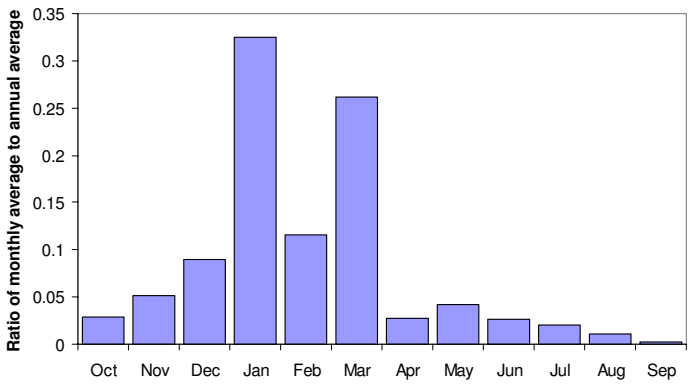

Figure 4.13 Average monthly flows in the Todd River expressed as percentages of annual average

As the available data extends over the period (1962-1998), it is possible to assess the variability in the ENSO signal through MEI data, which is only available from 1950 onwards. The method used to classify ENSO events with the MEI follows Kiem and Franks (2001) with values over six-month periods from October to March distinguishing annual ENSO phases. Kiem and Franks (2001) claim that this method is the most robust for identifying ENSO variability over the time period being investigated. In this manner, El Niño years are characterised by six-month MEI averages beginning the previous October being above 0.5 and La Niña events as years in which this average is below –0.5. Six-month averages of the IPO, provided in seasonal totals, are also used. The initial stage of this analysis is to use multiple linear regressions to relate ENSO phase to total annual flow. The total variability attributed to ENSO in the time series of annual flow is established through regressing flows on the MEI and IPO. Table 4.14 gives the coefficients (with standard errors) for regression models with the lowest standard deviation of residuals (in quantities of 1 x 10^6 m^3). The addition of a $MEI \times IPO$ term improves the regression, reducing the standard deviation of residuals from 17.73 to 16.02.

Table 4.14 Coefficients and standard errors (SE) for regression of total annual Todd flows on climate indices, with R^2 values, standard deviation of residuals (S) and overall P-values

Constant (SE)	Coefficient of MEI (SE)	Coefficient of IPO (SE)	Coefficient of MEI x IPO (SE)	R^2	S	P
9.80 (2.96)	**-2.62** (2.85)	**-2.93** (2.64)	**6.64** (2.27)	24.3 %	16.02	0.025

The next aspect of this study is to investigate the influence of ENSO upon discrete flow episodes. If the random processes underlying spate flows are considered the same from one year to the next, the distribution of annual spates would follow a Poisson distribution. The alternative considered is that the underlying processes depend on slowly varying global climate conditions that result in greater variability in the number of annual spates than are expected from a Poisson distribution. Table 4.13 indicates that the number of annual spates in the Todd is indeed overdispersed, with the ratio of variance to mean being 1.42. This overdispersion can be modelled through various approaches, the first of which through a Poisson regression function, including explanatory variables such as the MEI and the IPO. In this model, it is assumed that the dependent variable Y has a Poisson distribution given the independent variables $X_1, X_2, ..., X_m$, that is

$$P(Y = k \mid X_1, X_2, ..., X_m) = \frac{e^{-\mu}\mu^k}{k!} \quad k = 0,1,2,... \tag{4.6}$$

where μ is the mean of the Poisson process. The logarithm of this mean value is assumed to be a linear function of the explanatory variables, i.e.

$$\ln(\mu) = \alpha_0 + \alpha_1 X_1 + \alpha_2 X_2 + \ldots + \alpha_m X_m \quad \textbf{(4.7)}$$

The choice of a logarithm as the link function to relate the mean of the process to its predictor variables has the result of ensuring fitted values of μ remain positive. The deviance is a measure of the variability of Y, and if Y has a Poisson distribution, the expected value of the deviance will equal the degrees of freedom. Substantially larger values are evidence for Y being over-dispersed. Therefore, a best model is selected on the basis of smallest deviance.

By representing annual climate conditions as the average of climate index values over October to March periods, the model with the lowest deviance of residuals was

$$\ln(\mu) = 1.104 + 0.174 \times IPO \quad \textbf{(4.8)}$$

This equation, which was not improved by the inclusion of the MEI, produces a residual deviance of 54.41 on 35 degrees of freedom. As a result, for the time series of annual spates in the Todd, the MEI and IPO predictors are unable to sufficiently explain excess variability.

Although climate indices failed to be significant indictors of spate flows, ENSO impact is identified by expressing the modulation of ENSO phase by IPO through the nine climate categories shown in Table 4.11. For each annual period, the category corresponding to the specific combination of MEI and IPO in that year takes a value of one, with each of the other seven variables taking a value of zero. Poisson regressions for the time series of spates are now fitted with the eight indicator series, with Table 4.15 comparing the best models from using only the indices as predictors, with the best models obtained from fitting category indicators (shown in bold). The Akaike Information Criterion (Akaike, 1974) is used to compare the fit of each model, and shows that category predictors provide improved regression models than those based solely on climate indices. Although category predictors fail to explain all the excess variability in this time series, categories one and two represent La Niña conditions in IPO negative periods, and this is again consistent with results presented by Power *et al.* (1999a). This highlights that ENSO variability is responsible for most of the clustering of spates.

Table 4.15 Comparison of optimum Poisson regression models for number of annual spates in the Todd using six-month averages of MEI and IPO values as indicative of annual totals, and category indicator variables (shown in bold) as predictors

Best predictive models for $\ln(\mu)$ with standard errors of coefficients in brackets	Residual deviance	Degrees of freedom	AIC
1.104 + 0.174 x IPO (0.104) (0.088)	54.409	35	160.23
1.317 – 1.066 x **(ONE**or**TWO)** (0.094) (0.345)	45.508	35	151.33

4.3.2 Flows in African arid zone rivers

Analysis in the previous section demonstrated that ENSO variability influenced the occurrence and volume of discrete flow records in an arid-zone river in Australia. McMahon *et al.* (1992) demonstrated that the most variable flow regimes across the world were located in both Australia and southern Africa, so the flow records for two neighbouring arid zone rivers in the latter are now investigated. Cigizoglu *et al.* (2002) developed point process models to characterise the discrete flow episodes in the Omatako and Omaruru rivers in Namibia, although the roles of large-scale climatic regimes on such episodes were not considered. These rivers have flow conditions that are more extreme than those observed in the Todd, such that the influence of global climate fluctuations may be more clearly observed.

The Omatako and Omaruru Rivers are both located in the Kalahari Sandveldt of Namibia, southern Africa, as shown in Figure 4.14. Annual runoff rarely exceeds 10mm. Each river originates in the high central plateau of the country, with the Omatako flowing northeast as a tributary of the endoreic Okavango Basin, and the Omaruru flowing west to the Atlantic.

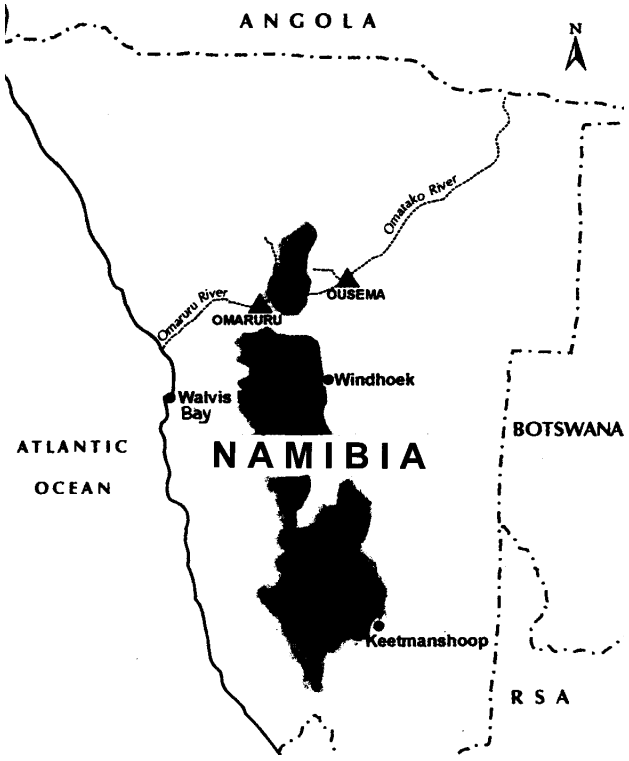

Figure 4.14 Locations of the Omatako and Omaruru rivers, together with their sampling sites shown as triangles (after Cigizoglu *et al.*, 2002)

Namibia has a subtropical desert climate, with ephemeral flow events in the Omatako and Omaruru confined generally to the wet season between January and April, which are also the hottest months. Mean daily flows are available for periods of 29 years (1962-1990) for the

Omatako River recorded at Ousema and 22 years (1965-1986) for the Omaruru recorded at the town of Omaruru. Summary statistics of these flow records are presented in Table 4.16.

Table 4.16 Summary flow statistics for the Omatako and Omaruru Rivers

River	Catchment (km^2)	Total annual flow ($x10^6$ m^3)				Number of annual spates	
		Minimum	Median	Mean	Maximum	Mean	Variance
Omatako	4970	1	20	35	144	4.45	5.61
Omaruru	2520	0	23	28	110	2.59	4.54

Periods of very little or zero flow in the Omatako and Omaruru are more exaggerated than in the Todd, with flow events having average durations of only 8.5 and 5.5 days respectively. The distinctive patterns of flow and the close association between these two rivers are shown in Figure 4.15 using two-year samples of daily flow.

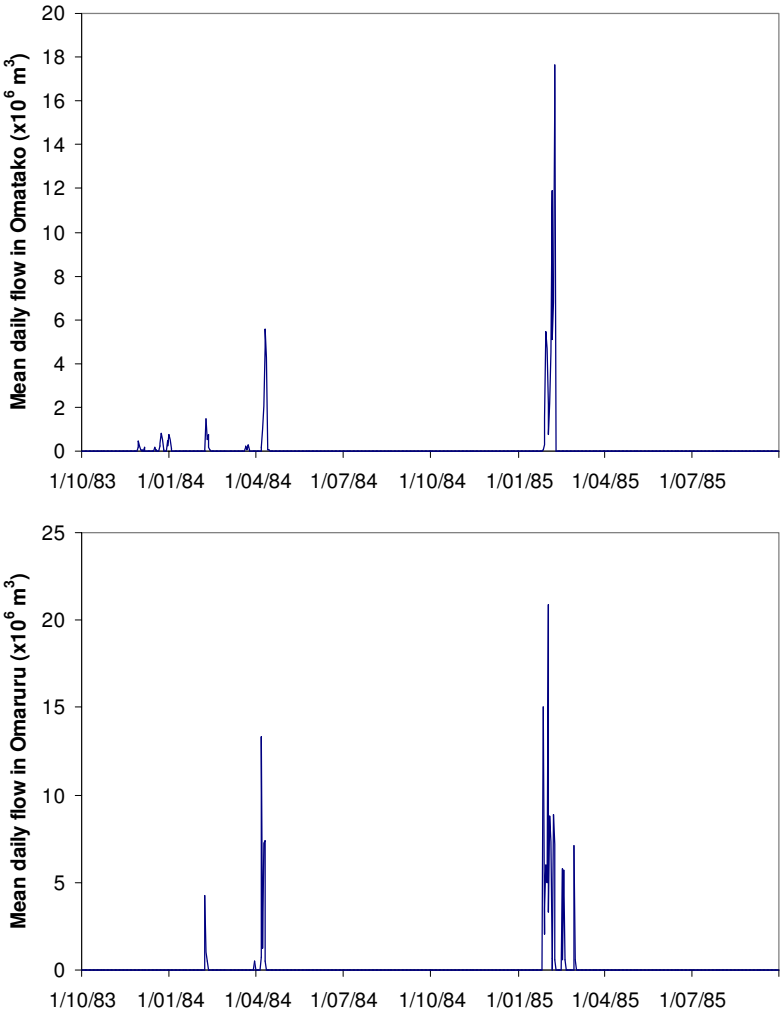

Figure 4.15 Daily flows in the Omatako and Omaruru Rivers (1983-1985)

Multiple linear regressions are used to relate ENSO phases to total annual flows in these two rivers, with the best regression models for each river summarised in Table 4.17. Although

ENSO indices fail to provide a significant description of annual flows in the Omaruru, a regression of the Omatako flows on the MEI explains over 20% of the variability in this series. Neither model was improved by the addition of a $MEI \times IPO$ term.

Table 4.17 Coefficients and standard errors (SE) for regression of annual flows in the Omatako and Omaruru on climate indices, with R^2 values, standard deviation of residuals (S) and P-values

River	Constant (SE)	Coefficient of MEI (SE)	Coefficient of IPO (SE)	R^2	S	P
Omatako	**35.49** (6.48)	**-17.43** (6.53)	–	20.9 %	34.89	0.013
Omaruru	**28.63** (6.12)	**-9.46** (6.42)	**8.06** (5.86)	13.3 %	28.60	0.259

The linear correlation of residuals from regression models of the Omatako and Omaruru (1965-1986) is 0.586, which is statistically significant $(p = 0.006)$. The regression of annual flows in both the Omatako and Omaruru on ENSO indices is now analysed in order to investigate the regional influence of ENSO, with a bivariate distribution describing the residuals. Therefore the natural logarithms of total annual flow in river *i*, $\ln(y_i)$, is assumed to follow the relationship

$$\ln(y_i) = \alpha_{0,i} + \alpha_{1,i} MEI + \alpha_{2,i} IPO + e_i \qquad \textbf{(4.9)}$$

where the residuals e_i are generated from a bivariate normal distribution. This equation uses the MEI and IPO as predictors of annual flows, although different coefficients for these predictors are estimated for each of the two rivers. The natural logarithm of flows produces marginal residuals that more closely approximate a series of random Gaussian variates. Table 4.18 shows coefficients for the best regression model from using combinations of predictor variables, together with the estimated correlation of the errors. This model has a regression constant and MEI coefficient that are identical for the two regression models, although different IPO coefficients are estimated. Importantly, this model explains more variability in these flow data than a standard bivariate normal distribution on the logarithm of flows.

Table 4.18 Coefficients and standard errors (SE) for optimum regression model of bivariate flow records, with bivariate normal distribution fitted to residuals for Omatako and Omaruru rivers

River	Correlation	Constant (SE)	Coefficient of MEI (SE)	Coefficient of IPO (SE)
Omatako	**0.785** (0.105)	**11.300** (5.740)	**-0.458** (0.221)	**-0.309** (0.207)
Omaruru				**-0.209** (0.412)

This result shows that annual flow volumes in these arid zone rivers are modulated by global circulation phenomenon. Although flow characteristics vary dramatically across these rivers, with the Omatako and Omaruru showing much shorter flow episodes and longer dry periods in

between such episodes than the Todd, ENSO still explains a large amount of flow. Furthermore, with the bivariate analysis providing an improved description of the relationship between streamflow and climate variability, it is evident that the regional extent of ENSO is important.

Modelling of spate flows in the two African rivers provides further evidence for the role of ENSO in modulating flow episodes in arid zones. Similar to the Todd, the numbers of annual spates in the Omatako and Omaruru are overdispersed, with the ratio of variance to mean being 1.26 in the Omatako and 1.75 in the Omaruru. By again representing annual climate conditions as the average index values over October to March periods, the model with the lowest standard deviation of residuals from fitting these predictors to the Omatako record was

$$\ln(\mu) = 1.456 - 0.284 \times MEI \qquad \textbf{(4.10)}$$

This equation, which was not improved by the inclusion of the IPO, produces a residual deviance of 26.96 on 27 degrees of freedom, consistent with the hypothesis of a Poisson variable. This can be compared with a residual deviance of 36.38 on 28 degrees of freedom for a null model without climate predictors, and corresponds to an R^2 of 25.9%. Consequently, the regression of MEI averages on the number of Omatako spates is regarded as a suitable fit, with this index alone explaining the excess variability in the Poisson-distributed response.

For the time series of annual spates in the Omaruru, the MEI and IPO predictors are unable to sufficiently explain excess variability, with residual deviance remaining in excess of the number of degrees of freedom. The best models from climate index predictors are now compared to Poisson regressions using the eight climate category series, with results summarised in Table 4.19. For the Omaruru, the best regression model on index values was not improved by the inclusion of the cross product of MEI and IPO, and the optimum model from fitting climate categories used a single one index that combined categories four, five and six. Categories four and five represent El Niño conditions, which is a similar result to that gained from the Omatako record. This again highlights that ENSO variability can explain most of the clustering of spates when arid zone rivers are modelled as individual series.

Table 4.19 Comparison of optimum Poisson regression models for number of annual spates in the Omatako and Omaruru Rivers using six-month averages of MEI and IPO values as indicative of annual totals, and category indicator variables (shown in bold) as predictors

River	Best predictive models for $\ln(\mu)$ with standard errors of coefficients in brackets	Residual deviance	Degrees of freedom	AIC
Omatako	**1.456** – **0.284** x MEI (0.091) (0.094)	26.962	27	124.37
	1.585 – **1.026** x **FIVE** (0.091) (0.389)	26.834	27	124.24
Omaruru	**0.935** – **0.259** x MEI + **0.237** x IPO (0.135) (0.154) (0.127)	38.241	19	95.87
	0.606 + **0.616** x **(FOUR**or**FIVE**or**SIX)** (0.212) (0.272)	36.993	20	92.62

The regional influence of ENSO upon isolated flows in these arid rivers will be more apparent if the observations from two rivers in the region are considered together. With the Omatako and Omaruru located in close vicinity, both rivers will be under similar climatic influences, and thus spate models may be improved by considering bivariate responses. A plausible model that allows for dependence within this pair of rivers is the bivariate Poisson distribution, as this retains a Poisson assumption for the number of annual spates recorded in each river, together with dependence between flows. A bivariate framework is fitted to annual spates in the African rivers over their common period (1965-1986), and allows for dependence between the Poisson-distributed variables Y_1 and Y_2, which have the expected values $E(Y_1) = \mu_1 = (\lambda_1 + \lambda_3)$ and $E(Y_2) = \mu_2 = (\lambda_2 + \lambda_3)$. The dependence between the variables is included in the model by the parameter λ_3, which is the covariance between Y_1 and Y_2. If λ_3 equals zero, the model reduces to the product of two independent Poisson distributions. The joint density of the bivariate Poisson distribution, as presented by Karlis and Ntzoufras (2003) is

$$P(Y_1 = y_1, Y_2 = y_2) = e^{-(\lambda_1+\lambda_2+\lambda_3)} \frac{\lambda_1^{y_1}}{y_1!} \frac{\lambda_2^{y_2}}{y_2!} \sum_{k=0}^{\min(y_1, y_2)} \binom{y_1}{k} \binom{y_2}{k} k! \left(\frac{\lambda_3}{\lambda_1 \lambda_2}\right)^k \quad \textbf{(4.11)}$$

The influence of ENSO on the spate occurrence is now incorporated by allowing the natural logarithm of the expected number of observations in river *i*, $\ln(\mu_i)$, to be a linear function of climatic predictors as shown in Eq. 4.12. This assumption is thus consistent with the univariate Poisson regression model.

$$\ln(\mu_i) = \alpha_{0,i} + \alpha_{1,i} MEI + \alpha_{2,i} IPO \qquad i = 1,2 \quad \textbf{(4.12)}$$

The dependence parameter λ_3 is estimated by the covariance between the annual numbers of spates in the two rivers, with remaining parameters fitted by a method of maximum likelihood.

Alternatively, the expectation-maximization algorithm developed by Karlis and Ntzoufras (2003) could also be used for parameter estimation. The Adaptive Metropolis algorithm (Haario *et al.*, 2001), described in Section 3.4 is also employed to evaluate parameter uncertainty in the form of posterior distributions for the set of unknown parameters.

The results from these bivariate Poisson calibrations are compared to those from independent models. The results in Table 4.20 show the optimum bivariate models from fitting ENSO indices, with Table 4.21 showing optimum models from using category predictors. Bayes Factors are included in each table comparing the optimum models to bivariate Poisson models with constant parameters. To maintain consistency with the results in Table 4.19, the category predictor for the Omatako and Omaruru combines categories four, five and six. These results indicate that the categories provide a slightly improved description of spate flows than the climate indices. Therefore models of bivariate flow patterns in both arid regions are improved by using indicators of ENSO variability and its multi-decadal modulation.

Table 4.20 Coefficients and standard errors (SE) for optimum bivariate Poisson models, using climate indices as predictors, and Bayes Factors from comparing to fixed parameter models

River	Constant (SE)	Coefficient of MEI (SE)	Coefficient of IPO (SE)	ln *BF*
Omatako	**1.465** (0.106)	**-0.214** (0.111)	**-0.144** (0.099)	**1.78**
Omaruru	**0.936** (0.135)	**-0.266** (0.150)	**0.234** (0.126)	

Table 4.21 Coefficients and standard errors (SE) for optimum bivariate Poisson models, using climate categories as predictors, and Bayes Factors from comparing to fixed parameter models

River	Constant (SE)	Coefficient of **categories (4 or 5 or 6)** (SE)	ln *BF*
Omatako	**1.660** (0.125)	**-0.419** (0.211)	**4.75**
Omaruru	**0.608** (0.208)	**0.632** (0.272)	

4.4 Summary of chapter

This chapter has investigated relationships between large-scale climatic variability, as identified by various climate indices, and variability in both rainfall and streamflow data. Deseasonalised monthly hydrologic data were used in these analyses, as the monthly scale was useful in the detection of the dominant frequency of ENSO fluctuations.

Using spatially-averaged rainfall data, it is apparent that monthly rainfall across much of Australia is modulated by the opposite phases of both the ENSO and IPO phenomena. Inevitably those districts in which monthly rainfall is not modulated significantly by Pacific climate modes, show a significant relationship to variability in Indian Ocean SSTs. Correlations between monthly rainfall and the first principal component from the NINO3, IPO and DMI series were stronger than correlations to the NINO3 alone in a majority of meteorological

districts, indicating the usefulness of this technique to represent an overall impact of these three climate phenomena.

Monthly streamflows demonstrated stronger relationships to climate indices than the spatially-averaged rainfall data, with the NINO3 being a more significant predictor than the PC_1 series in data from the longest rivers, suggesting a strong relationship between ENSO and streamflow. These correlations are stronger than those observed with rainfall due to the aggregation that occurs in rainfall-runoff transformations. The combined influence of ENSO and IPO were also analysed through the use of monthly climate indicator categories, and importantly the dominant category reflected La Niña episodes in IPO negative epochs. Flow data from three arid-zone rivers are also analysed, with results demonstrating clear teleconnections with ENSO variability. With both the rate of occurrence and the volume of short flow episodes in arid zone rivers being influenced by ENSO, existing hydrological models for such rivers may be improved through incorporating both the ENSO and the IPO predictors. An alternative explanation for the overdispersion of spate numbers is through persistence in the annual flow regime that is related directly to low-frequency climate variability. This chapter demonstrates that climate indices are a useful mechanism to represent changes within persistent climate modes, and to relate climatic persistence to hydrological data. In the following chapter, the relationship between persistent climate modes and hydrologic data is examined further through spells analysis.